

Autonomous hanging tether management and experimentation for an unmanned air-surface vehicle team

Kurt Talke^{1,2} | Frederick Birchmore³ | Thomas Bewley²

¹Unmanned Systems Advanced Development Branch, Naval Information Warfare Center Pacific, San Diego, California, USA

²Department of MAE, UC San Diego, La Jolla, California, USA

³Autonomous ISR Branch, Naval Information Warfare Center Pacific, San Diego, California, USA

Correspondence

Kurt Talke, Unmanned Systems Advanced Development Branch, Naval Information Warfare Center, Pacific, San Diego, CA 92110, USA.

Email: kurt.a.talke.civ@us.navy.mil and ktalke@ucsd.edu

Funding information

Department of Defense SMART Scholarship for Service program; Naval Information Warfare Center Pacific under the Naval Innovative Science and Engineering program

Abstract

The mission of an unmanned air vehicle (UAV) tethered to a small unmanned surface vehicle (USV) is considered. As opposed to the majority of existing tethered UAV work, which assumes a taut tether, this paper addresses the challenge of tether management for a slack, hanging tether in a dynamic ocean environment up to sea state 4 on the Douglas scale. A prototype smart reel system for a UAV-USV team was designed and experimentally validated in controlled and uncontrolled dynamic environments. A reference model for tether control based on static catenary cable theory was extended and shown to be valid through the entire operational envelop. A Kalman filter was developed to fuse slow (4 Hz) differential GPS (dGPS) relative position measurements with fast (100 Hz) inertial measurements, to output a 100 Hz estimate of relative position, relative velocity, and inertial sensor bias. A relative velocity-based gain-scheduled proportional-derivative (PD) controller was developed, and demonstrated robustness to heave, pitch, and roll motion of the USV. Experimental testing with a UAV surrogate showed successful decoupling of heave motion from the UAV altitude in a controlled indoor environment. Taut tether control, in contrast, exhibited 12 times more tether tension at the UAV compared to the controller proposed here. The performance of the tuned controller with feedback from the Kalman filter exhibited minimal deviation from static catenary cable theory during the dynamic experiments. Indoor flight testing showed the developed reference model and controller essentially decoupled the dynamic motion of the USV from that of the UAV; the measured deflections of the UAV altitude and position essentially matched that of untethered flight. Outdoor flights validated the effectiveness of the controller in an unknown dynamic environment, for a larger relative position between the UAV and USV, using the dGPS Kalman filter solution to measure relative position. Initial experimental results look promising for continued on-water testing of hanging-tether UAV/USV teams.

KEY WORDS

field robotics, multirobot cooperation, UAVs, unmanned surface vehicle

1 | INTRODUCTION

A significant limitation of multirotor unmanned air vehicle (UAV) flight is the short mission duration due to battery life and payload capacity, often limited to less than 30 min flight time (Kim et al., 2013). This compounds when trying to use the UAV to perform tasks involving a high-power radio. The heavier the payload, the greater thrust required, and the shorter the mission. To overcome such challenges, a recent trend has been to provide power over an umbilical tether, thus enabling essentially unlimited flight duration (Choi et al., 2014; Papachristos & Tzes, 2014; Sandino, Bejar, et al., 2014). Unfortunately, a tether limits the mobility of the UAV, and introduces the challenge of active tether management. Also, tethered flight introduces additional downward forces on the UAV due to tether weight and tension. These forces must be overcome by increasing UAV thrust, potentially reducing the UAV payload capacity and available power budget. The majority of tethered UAV work considers only the taut tether case, to avoid tether oscillations (Schmidt & Swik, 1974), improve flight stability (Ferreira de Castro et al., 2015; Lupashin & D'Andrea, 2013; Nicotra et al., 2014; Ouchi et al., 2014; Sandino et al., 2013), or enhance landing capability (Ahmed & Pota, 2008; Oh et al., 2006; Sandino, Santamaria, et al., 2014). Such systems neglect the reduced payload capacity and increased UAV thrust requirement. They employ either no tether management while the UAV maintains tension with linear and nonlinear flight controllers (Nicotra et al., 2014, 2016), or a tension monitoring winch mechanism that continuously reels in any slack tether length (Briggs & Stave, 2017). Other systems have considered non-taut tethered flight using a reactive tether management approach (Zikou et al., 2015). The addition of a tether to a UAV gives the potential of additional measurable quantities (rotational position and velocity of the reel, and tension of the tether) upon which non-GPS based UAV position estimation may be performed. The tether arrival angle at the UAV is measured (Sandino et al., 2015), and/or the tension at the UAV estimated (Al-Radaideh & Sun, 2017), and incorporated into the state estimation algorithm. Other prior related work has used a non-taut catenary cable model for position estimation (Galea & Kry, 2017; Kiribayashi et al., 2017). These tethered systems consider only a scenario where the base station is stationary, not undergoing dynamic motion as considered here. Other work has considered tethered UAVs with moving platforms, but under taut conditions, and with no experimental validation (Tognon et al., 2016).

The mission schematic for a tethered UAV system considered here is shown in Figure 1. The UAV, flying at up to 50 m altitude, must maintain position, orientation, and altitude for communication or intelligence, surveillance, and reconnaissance (ISR) missions. The UAV is tethered to a small, 3–7 m length unmanned surface vehicle (USV) subject to a dynamic ocean environment. Providing power over an umbilical tether enables long-duration UAV flight over 22 hours (Prior, 2015). However, the total system power budget is limited for small USVs in long-duration missions. Compared to taut-tether UAV operation, the use of a hanging tether can minimize the downforce that the tether applies to the UAV, ultimately decreasing power consumption by the UAV-USV team, while maintaining the required margins of safety on the thrust of the UAV. The fast-acting dynamics of an ocean environment are inherently compensated for

through the varying sag of the tether. Flying on a non-taut, or hanging tether can effectively decouple the motion of the UAV and the USV, but introduces two potential failure mechanisms during large heave events which must be solved by appropriate tether management: (i) preventing the tether going taut, and thus pulling down on the UAV, and (ii) preventing the tether from dipping down to the ocean surface, and thus likely fouling on the USV.

In this paper, a tether management prototype design, relative position estimator, and control system for autonomous tether management are developed. Experimental testing validated the design through indoor motion capture-based experimentation and outdoor real-time kinematic (RTK) differential GPS (dGPS)-based experimentation. Indoor experimentation, using a UAV surrogate for a perfectly known, controlled environment, demonstrated the developed estimator and controller greatly reduce tether tension and forces on the UAV compared to taut tether control. Indoor flight testing successfully decoupled the USV heave motion from the UAV altitude and position deviations, while demonstrating a UAV altitude and position variability range that was comparable to that obtained in untethered flight. Finally, outdoor flight testing using a Kalman filter solution leveraging dGPS and an inertial measurement unit (IMU), to determine relative position, demonstrated the feasibility of our approach in an unknown dynamic environment, thus establishing that a hanging tether management system can indeed extend mission duration, decrease power consumption, and increase operating altitude.

This paper is organized as follows: Section 2 details the tether management prototype, estimation, and control methods. Section 3 describes the experimental setup. Section 4 presents and discusses experimental results. Section 5 summarizes the key conclusions.

2 | AUTONOMOUS TETHER MANAGEMENT PROTOTYPE

For a tether management system to function outside of a lab environment, it needs to be able to control and measure tether length, provide tether tension or motor torque feedback, measure the tether departure angle, and provide appropriate safety margins to prevent catastrophic forces on the UAV. For future UAV payloads of interest, a coaxial tether with a diameter of 4.5 mm is used here, which is significantly larger than typical tethers used in existing tethered UAV systems. The tether management problem is challenging due to the substantial weight and bending stiffness of the tether itself. Our analysis of the design and performance of the tether management system is primarily divided among four main subsystems: mechanical design, controller design, catenary tether model, and estimator design.

2.1 | Mechanical design

A prototype smart reel system, similar to the non-taut tether management system found in previous work (Zikou et al., 2015), is shown in Figure 2. The prior work used a torsional spring to measure

FIGURE 1 Schematic of a tethered UAV-USV team in an ocean environment with waves up to sea state 4. The smart reel system controls tether length to account for the dynamic motion of the small USV, leaving the tether in a semislack, quasi-static state at all time. UAV, unmanned air vehicle; USV, unmanned surface vehicle. [Color figure can be viewed at wileyonlinelibrary.com]

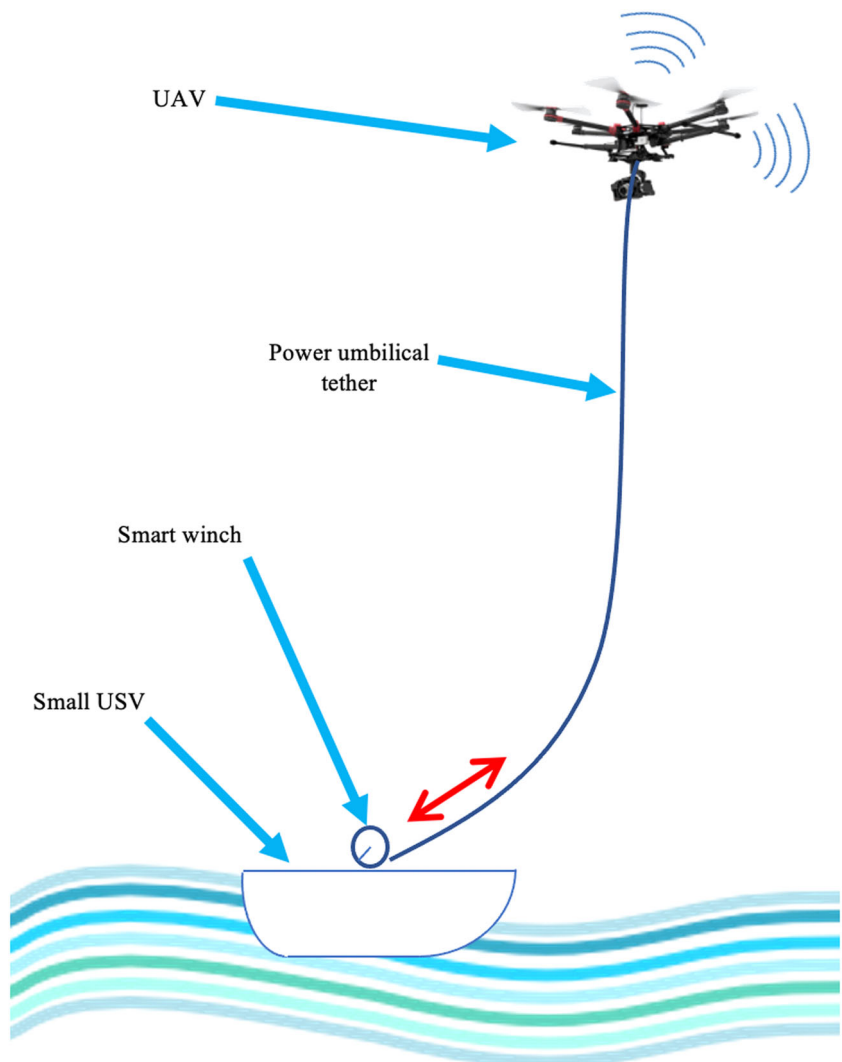
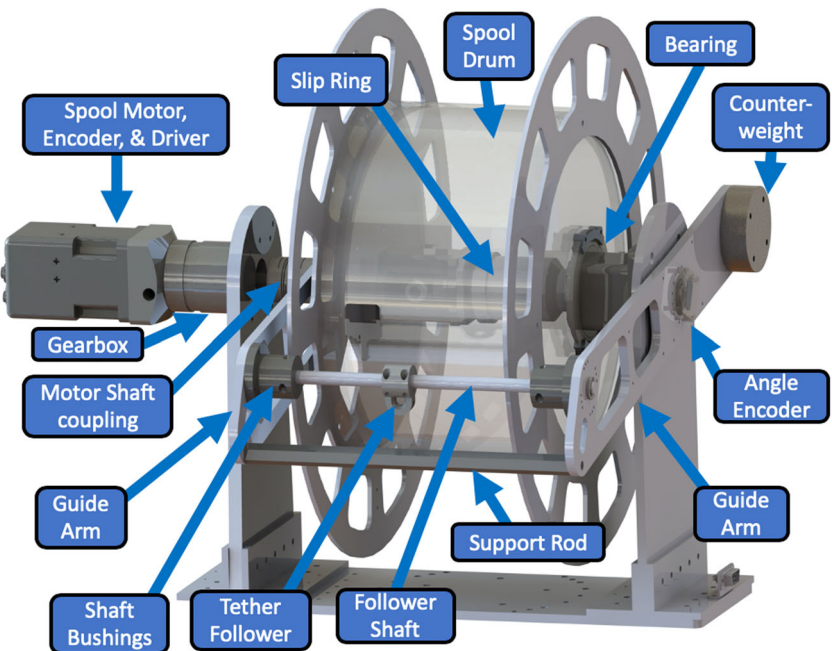


FIGURE 2 Smart reel prototype capable of spooling 100 m of 4.5 mm diameter tether with a 50 mm minimum bend radius. The integrated sensors can measure the tether length, departure angle, and motor torque. [Color figure can be viewed at wileyonlinelibrary.com]



torque, and a noncontact proximity sensor to measure the departure angle of the tether. Our design differs from earlier designs by using the motor current to measure motor torque and using a balanced, contact-based passive tether follower to measure the departure angle of the tether. One of the goals of the experimental approach described in Section 3 is to characterize this unique angle measurement approach and its feasibility as a means for feedback. As the tether exits the spool, it feeds through a tether follower attached to guide arms. The follower is free to slide left and right along a shaft as needed for spool winding. The guide arms can rotate freely about the spool. A support rod constrains the two guide arms to rotate together. The guide arms are counter-weighted such that the weight of the arm does not affect the departure angle of the tether. An absolute encoder on the guide arm measures the angular rotation of the guide arm. The balanced freedom of movement of the follower allows for a minimally intrusive measurement of the tether departure angle. A future design improvement will be to convert the follower and follower shaft into a cross-threaded level winding screw to spool neatly and accommodate greater tether lengths for large deployment or retrieval. A motor-encoder-gearbox combination connects directly to a slip ring inside the spool drum through a drive shaft and coupling. The slip ring transfers the required power at 400 V and communication signals to allow the spool to spin up to 100 rpm, while also providing the necessary power for sustained UAV flight. A future design improvement will be to incorporate a turntable to allow the entire system to rotate, thereby ensuring the smart reel stays pointed at the UAV.

2.2 | Controller design

For the tether management prototype, a dynamic gain-scheduled discrete-time proportional-derivative (PD) controller running at 50 Hz is graphically shown in Figure 3. The controller inputs are the estimated relative altitude, $\Delta\tilde{z}_k$, the estimated relative vertical velocity, $\Delta\dot{\tilde{z}}_k$, the measured tether length, L_k , and a slow, 4 Hz, relative radial distance measurement, Δr_k . An error signal, e_k , and its derivative, multiplied by the proportional and derivative gains, K_p and K_d , respectively, are used

to determine the commanded motor voltage, u_k , the controller input. The gains change depending on the relative velocity between the UAV and USV, with both the gains and velocity thresholds found through experimental testing. The error signal is generated using the difference between the measured tether length, L_k , and a gain-scheduled low-pass filtered reference tether length $L_{ref,k}^{LP}$. The low-pass filter is a typical first order discrete-time filter defined as:

$$L_{ref,k}^{LP} = (1 - \alpha)L_{ref,k-1}^{LP} + \alpha L_{ref,k}, \quad (1)$$

where $\alpha \in [0, 1]$ is the filter smoothing factor and scheduled depending on how fast the relative altitude changes. The intent of the low-pass filter is to smooth out the reference tether length, $L_{ref,k}$, due to any discontinuities in the relative altitude estimate at slow speeds. At high relative velocities, the relative altitude estimate proved experimentally to be smooth, and α was set to 1 to pass through the reference tether length without filtering it. The gain-scheduler is set up similar to an electronic Schmitt trigger, where the threshold for triggering between states changes depending on specific criteria (Schmitt, 1938). Determined experimentally, an α value of 0.2 was used when the relative velocity dropped below 0.3 m/s. If the relative velocity dropped below 0.1 m/s, the threshold would also drop down to 0.1 m/s. This has the effect of smoothly transitioning to a low-pass filtered reference signal when the relative velocity slows down, but abruptly turning off the filter with increasing relative velocity, allowing for the smart reel to respond faster without the low-pass filter-induced lag. The reference tether length, determined by a catenary tether-based heave model previously developed, is dependent on the relative altitude estimate and relative radial distance (Talke et al., 2018). Our previous work investigated the heave model based on static catenary hanging cable theory but did not experimentally validate the model for control of a hanging tether from a dynamically moving UAV or USV.

2.3 | Catenary tether model

This section will summarize the catenary tether-based heave model developed in our previous work (Talke et al., 2018), and

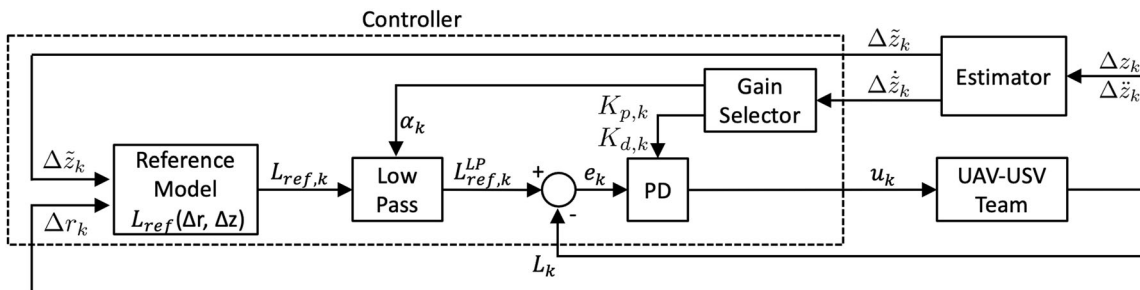


FIGURE 3 Tether management controller. The relative position of the UAV and USV feed into the polynomial model to determine a reference length. Comparison to the measurement estimate from the spool encoder creates an error signal. A PD controller on the spool motor commands the spool to pay out or reel in tether. The low-pass filter coefficient and the controller gains are gain-scheduled-based on the estimated relative velocity. PD, proportional derivative; UAV, unmanned air vehicle; USV, unmanned surface vehicle.

extend its valid operation range. The static catenary cable equation given by:

$$z = z_0 + a \cosh\left(\frac{r - r_0}{a}\right) = z_0 + \frac{a}{2} \left(e^{\frac{r-r_0}{a}} + e^{-\frac{r-r_0}{a}} \right), \quad (2)$$

where z is the altitude or height along the catenary curve, r the radial distance, z_0 and r_0 are the coordinate offset variables, and a is the catenary parameter, was converted to relative position form:

$$\sqrt{L^2 - \Delta z^2} = 2a \sinh\left(\frac{\Delta r}{2a}\right), \quad (3)$$

where Δr and Δz are the radial and vertical distance between the UAV and the USV, and L is the known tether length. Because Equation (3) is a transcendental equation in a , it was empirically analyzed for a range of operating conditions from 0 to 60 m in radial distance and altitude, and varying range of tether lengths. For each relative position, a heave robustness tether shape was determined that allows for equal vertical heave displacement of the USV to specified tension and sag limits while the tether length remains unchanged. The results of the empirical analysis were curve fitted to develop a reference model for tether length, departure angle, and tension, depending only on the relative position between the UAV and USV. A key result from the analysis was a recommended operating relative position ratio, $\Delta r/\Delta z \approx 0.46$. In this study, only the length model will be used, and the simple third-order polynomial is repeated here for reference:

$$L_{ref} = \Delta z \left(c_1 + c_2 \frac{\Delta r}{\Delta z} + c_3 \frac{\Delta r^2}{\Delta z^2} + c_4 \frac{\Delta r^3}{\Delta z^3} \right) \quad (4)$$

with coefficients $c_1 = 0.9964$, $c_2 = 0.1514$, $c_3 = 0.4674$, and $c_4 = -0.1280$. The third-order model was originally developed for $\Delta r/\Delta z \leq 1.2$. In that region, the third-order approximation is nominally better than a lower-order model. However, outside the region, because this model is third order, it has an inflection point, which occurs at $\Delta r/\Delta z = 1.22$. For $\Delta r/\Delta z > 1.22$, the third-order model is no longer physical, and results in a fully taut tether reference length at $\Delta r/\Delta z = 1.77$. While the goal is to operate at $\Delta r/\Delta z < 1$, the

constrained indoor testing environment and other operation scenarios can result in $\Delta r/\Delta z > 1.2$. A second-order curve fit model, extrapolated from the third-order model, will be used for such operation regions:

$$L_{ref} = \Delta z \left(d_1 + d_2 \frac{\Delta r}{\Delta z} + d_3 \frac{\Delta r^2}{\Delta z^2} \right) \quad (5)$$

with coefficients $d_1 = 0.9748$, $d_2 = 0.2615$, and $d_3 = 0.2370$. The original third-order model and the extrapolated second order curve fit model are show in Figure 4. For relative position ratio, $\Delta r/\Delta z \leq 1.1$, the third-order model will be used, and for $\Delta r/\Delta z \geq 1.3$, the second-order model will be used. In the region between, $1.1 < \Delta r/\Delta z < 1.3$, a linear combination of the second and third-order models is used to smooth the transition as seen in Figure 4b. A key challenge for this control approach will be the accurate measurement of relative position.

2.4 | Sensing and estimation filter design

To address the challenge of determining the relative position, a commercial off-the-shelf RTK dGPS solution is used. However, RTK dGPS solutions are limited to a maximum 4 Hz update rate, which is too slow for the developed controller, which runs at 50 Hz. To augment the estimated relative position during the time in between RTK dGPS measurements, a Kalman filter model was designed to measure and double integrate the acceleration using two inertial measurement units (IMUs) running at 100 Hz. There are numerous examples of GPS-inertial navigation system (INS) Kalman filters for a variety of applications (Carvalho et al., 1997; Qi & Moore, 2002; Simon, 2006; Thrun et al., 2005), as well as some more specific to using RTK dGPS and UAV navigation (Gross et al., 2015; Oh, 2010; Schall et al., 2009; Suh et al., 2017). To simplify for this scenario, the Kalman filter is restricted to the altitude degree of freedom (DOF) since the primary DOF affecting the tether is the vertical heave motion of the USV, and the UAV is near hover. To account for the bias due to gravity of the

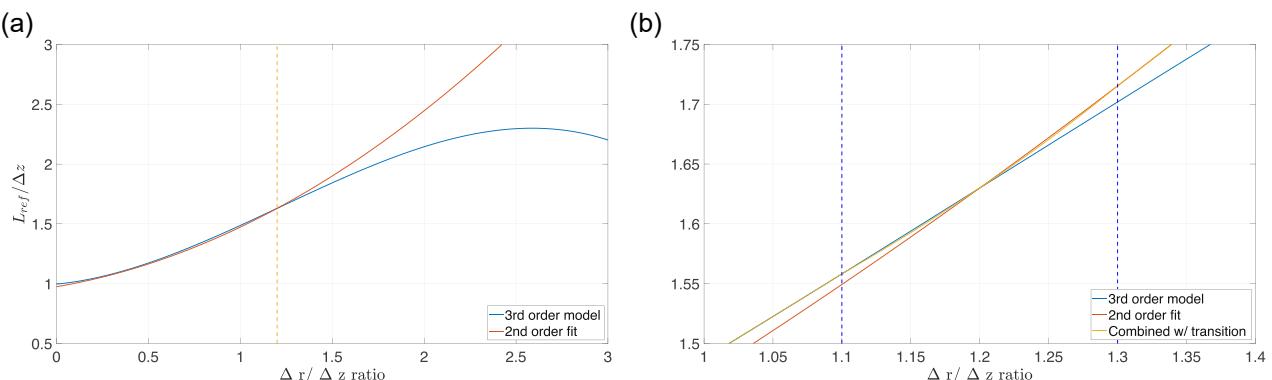


FIGURE 4 Tether reference model showing (a) the third-order model, its inflection point, and the second-order fit for relative position ratio $\Delta r/\Delta z > 1.2$ and (b) a closeup of the linear combination of both models in the transition region between $1.1 < \Delta r/\Delta z < 1.3$. [Color figure can be viewed at wileyonlinelibrary.com]

accelerometers, they are included in the double integration dynamic model for the Kalman filter as:

$$X = \begin{bmatrix} \Delta z \\ \Delta \dot{z} \\ \Delta \ddot{z} \\ \mu_1 \\ \mu_2 \end{bmatrix}, X_{k+1} = \begin{bmatrix} 1 & \Delta t & 0 & 0 & 0 \\ 0 & 1 & \Delta t & 0 & 0 \\ 0 & 0 & 1 & 0 & 0 \\ 0 & 0 & 0 & 1 & 0 \\ 0 & 0 & 0 & 0 & 1 \end{bmatrix} X_k + \begin{bmatrix} \omega_{z,k} \\ \omega_{\dot{z},k} \\ \omega_{\ddot{z},k} \\ \omega_{\mu_1,k} \\ \omega_{\mu_2,k} \end{bmatrix} \quad (6)$$

such that:

$$\begin{aligned} \Delta z_{k+1} &= \Delta z_k + \Delta t \Delta \dot{z}_k + \omega_{z,k} & \omega_z &= N(0, \sigma_z^2) \\ \Delta \dot{z}_{k+1} &= \Delta \dot{z}_k + \Delta t \Delta \ddot{z}_k + \omega_{\dot{z},k} & \omega_{\dot{z}} &= N(0, \sigma_{\dot{z}}^2) \\ \Delta \ddot{z}_{k+1} &= \Delta \ddot{z}_k + \omega_{\ddot{z},k} & \omega_{\ddot{z}} &= N(0, \sigma_{\ddot{z}}^2) \\ \mu_{1,k+1} &= \mu_k + \omega_{\mu_1,k} & \omega_{\mu_1} &= N(0, \sigma_{\mu_1}^2) \\ \mu_{2,k+1} &= \mu_k + \omega_{\mu_2,k} & \omega_{\mu_2} &= N(0, \sigma_{\mu_2}^2) \end{aligned} \quad (7)$$

where Δz , $\Delta \dot{z}$, $\Delta \ddot{z}$ are the relative position, velocity, and acceleration, respectively, μ_1 and μ_2 are the estimated accelerometer biases, and Δt is the timestep of the filter running at 100 Hz. All states are assumed to have zero mean and normally distributed system noise.

The measurement model is defined as:

$$Y_k = \begin{bmatrix} \Delta z_{dGPS} \\ \Delta \ddot{z}_{Acc1} \\ \Delta \ddot{z}_{Acc2} \end{bmatrix}, Y_k = \begin{bmatrix} 1 & 0 & 0 & 0 & 0 \\ 0 & 0 & 1 & 1 & 0 \\ 0 & 0 & 1 & 0 & 1 \end{bmatrix} \begin{bmatrix} \Delta z_k \\ \Delta \dot{z}_k \\ \Delta \ddot{z}_k \\ \mu_{1,k} \\ \mu_{2,k} \end{bmatrix} + \begin{bmatrix} v_{z,k} \\ v_{\dot{z}_1,k} \\ v_{\dot{z}_2,k} \end{bmatrix} \quad (8)$$

such that:

$$\begin{aligned} \Delta z_{dGPS,k} &= \Delta z_k + v_{z,k} & v_z &= N(0, \sigma_{dGPS}^2) \\ \Delta \ddot{z}_{Acc1,k} &= \Delta \ddot{z}_k + \mu_{1,k} + v_{\dot{z}_1,k} & v_{\dot{z}_1} &= N(0, \sigma_{Acc1}^2) \\ \Delta \ddot{z}_{Acc2,k} &= \Delta \ddot{z}_k + \mu_{2,k} + v_{\dot{z}_2,k} & v_{\dot{z}_2} &= N(0, \sigma_{Acc2}^2) \end{aligned} \quad (9)$$

where Δz_{dGPS} is the RTK dGPS measurement, and $\Delta \ddot{z}_{Acc1}$ and $\Delta \ddot{z}_{Acc2}$ are the vertical accelerations from both IMUs. All measurements are assumed to have zero mean, normally distributed measurement noise. Some care needs to be taken due to the fact that the RTK dGPS measurement is slow, at 4 Hz. During the time between RTK dGPS measurements, the dGPS standard deviation, σ_{dGPS} , is artificially set to infinity to zero out the Kalman gain for that state.

3 | EXPERIMENTAL TESTING PROCEDURE

The experimental testing procedure is split into three stages to first validate the controller and mechanical prototype, tune and validate the estimation filter, and then evaluate the RTK dGPS solution:

1. UAV surrogate testing is performed to validate the controller. To accomplish this, a 120 Hz infrared camera motion capture

(MoCap) system is used for relative position feedback to validate the controller and tune the estimation filter. Then, the estimation filter is evaluated, derating the MoCap system feedback down to 4 Hz to replicate the RTK dGPS measurement.

2. Indoor flight testing is performed to introduce the dynamic variability of the UAV, again using the MoCap system and the estimation filter for relative position feedback.
3. Outdoor flight testing is performed using the RTK dGPS as input into the estimation filter for relative position feedback.

This staged approach will first evaluate the tether reference model, the controller, and the mechanical prototype in a controlled environment, then involve flight dynamics with perfect feedback, then incorporate the estimation filter for increased complexity and difficulty, and finally evaluate the feasibility of the RTK dGPS sensor for feedback. For each of the scenarios described, the smart reel is mounted onto the payload platform of a 3-PSR mechanism to replicate wave and boat motion (Talke et al., 2019). The sensor subsystem communication design and wave profiles are discussed after the test setup for each scenario.

3.1 | UAV surrogate test setup

A rigidly mounted load sensor acting as a UAV surrogate was used to evaluate and validate the tether model and controller before flying. The UAV surrogate was rigidly mounted just beneath the 7 m high ceiling of the testing facility as shown in Figure 5.

The tether was mounted to a rotating connector which measures the arrival angle, β , with a potentiometer. A fulcrum converts the tension load into compression for the load cell to measure the vertical component of the tether tension. Using the angle and vertical load, the geometry of the fulcrum determines the tether tension. A microprocessor was used to read the load and angle data and communicate it to the smart reel for data logging purposes. The wave mechanism was positioned in such a way that the relative position is at the recommended ratio $\Delta r/\Delta z = 0.46$ when the platform is at the bottom of its range (Talke et al., 2018). The 3-PSR wave replication mechanism runs a prescribed wave profile in open loop in three DOFs: pitch, roll, and heave. The MoCap system was used for ground truth feedback, and then de-rated to tune and evaluate the estimation filter. Next, a comparative test evaluated the controller against a typical taut controller. The taut controller maintained a specified torque on the spool, reeling in and paying out as needed to maintain tension on the tether.

3.2 | Filter tuning

The time-series data obtained while validating the controller was then used to tune the estimation filter. The ad-hoc so-called "Twiddle Algorithm" was used to refine the Kalman filter standard deviation values (Abbeel et al., 2005; Thrun, 2012). In this application, the

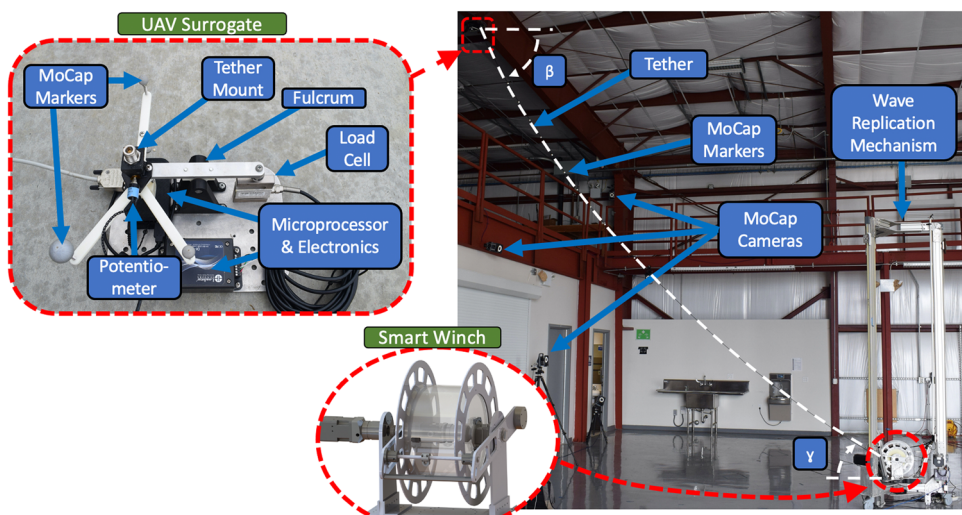


FIGURE 5 UAV surrogate test setup during taut tether testing. The smart reel prototype is mounted on the 3-PSR wave replication mechanism. The tether is highlighted with a white dashed line to make it more visible. The UAV surrogate components are labeled, as well as the tether departure and arrival angles, γ and β . UAV, unmanned air vehicle. [Color figure can be viewed at wileyonlinelibrary.com]

“Twiddle Algorithm” runs the Kalman filter over the time series data given an initial nominal set for the standard deviations, P . A metric, Q , specified by the root mean square error (RMSE) between the measured relative position from the MoCap and the estimated relative position from the filter, $\Delta\tilde{z}$, quantifies the cost of the standard deviation set. Subsequently, the algorithm loops over all the standard deviation values, increasing and decreasing, or “twiddling” each by an amount, $\delta\sigma_i$. The cost is then recalculated based on the time-series data, keeping the standard deviation set with the lowest, or best cost. The amount to “twiddle” the standard deviation, $\delta\sigma_i$, is then increased by 10%, with the caveat that it can be no greater than half of the current standard deviation. If the “twiddle” of the standard deviation variable does not lower the cost, $\delta\sigma_i$ is decreased by 10%. The “twiddle” process is then repeated until an acceptance criteria is reached. In this case, the criteria is the convergence of the sum of the proportion of $\delta\sigma$ to σ to less than 10%. In summary, the algorithm “twiddles” the standard deviations, increasing or decreasing each variable in turn until the cost converges. Psuedocode for the modified Twiddle Algorithm is shown in Algorithm 1.

Algorithm 1 Modified Twiddle Algorithm

```

1:  $P = [\sigma_z, \sigma_{\dot{z}}, \dots, \sigma_{Acc_2}]$ 
2:  $dP = [\delta\sigma_z, \delta\sigma_{\dot{z}}, \dots, \delta\sigma_{Acc_2}]$ 
3:  $m = \text{length}(P)$ 
4:  $n = \text{length}(\text{data})$ 
5:  $\Delta\tilde{z} = \text{kfilter}(P, \text{data})$ 
6:  $Q_{Best} = \sqrt{\frac{1}{n} \sum_{j=0}^n (\Delta\tilde{z}_j - \Delta z_j)^2}$ 

```

```

7:  $l = 1$ 
8:  $\text{while } \frac{1}{m} \sum_{j=0}^m (dP_j/P_j) > .1 \text{ do}$ 
9:    $\text{for } i = 1 : m \text{ do}$ 
10:     $P(i) = P(i) + dP(i)$ 
11:     $\Delta\tilde{z} = \text{kfilter}(P(i), \text{data})$ 
12:     $Q_l = \sqrt{\frac{1}{n} \sum_{j=0}^n (\Delta\tilde{z}_j - \Delta z_j)^2}$ 
13:     $\text{if } Q_l < Q_{Best} \text{ then}$ 
14:       $Q_{Best} = Q_l$ 
15:       $\text{if } dP(i)/P(i) <= 0.5 \text{ then}$ 
16:         $dP(i) = dP(i)*1.1$ 
17:       $\text{else}$ 
18:         $dP(i) = P(i)*0.5$ 
19:       $\text{end if}$ 
20:     $\text{else}$ 
21:       $P(i) = P(i) - 2*dP(i)$ 
22:       $\Delta\tilde{z} = \text{kfilter}(P(i), \text{data})$ 
23:       $Q_l = \sqrt{\frac{1}{n} \sum_{j=0}^n (\Delta\tilde{z}_j - \Delta z_j)^2}$ 
24:       $\text{if } Q_l < Q_{Best} \text{ then}$ 
25:         $Q_{Best} = Q_l$ 
26:         $\text{if } dP(i)/P(i) <= 0.5 \text{ then}$ 
27:           $dP(i) = dP(i)*1.1$ 
28:         $\text{else}$ 
29:           $dP(i) = P(i)*0.5$ 
30:         $\text{end if}$ 
31:       $\text{else}$ 
32:         $P(i) = P(i) + dP(i)$ 
33:         $dP(i) = dP(i)*0.9$ 
34:       $\text{end if}$ 
35:     $\text{end if}$ 
36:   $\text{end for}$ 
37:   $l = l + 1$ 
38:  $\text{end while}$ 

```

(Continues)

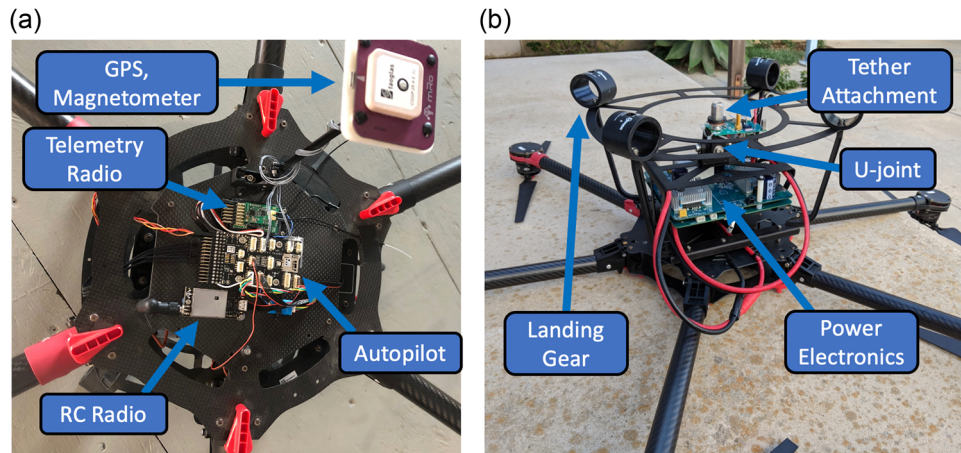


FIGURE 6 UAV test setup. (a) Topside of the UAV showing flight electronics. (b) Underside of the UAV showing the tether attachment point and power electronics. UAV, unmanned air vehicle. [Color figure can be viewed at [wileyonlinelibrary.com](#).]

3.3 | Indoor flight test setup

For indoor flight testing, the UAV surrogate is replaced with a modified DJI S900 hexacopter UAV shown in Figure 6. The UAV is flown in remote control (RC) mode with an open source ArduPilot flight controller. The UAV uses a Pixhawk autopilot, RC and telemetry radios, GPS for outdoor flight, magnetometer, power electronics, and have a tether mounting point on a u-joint to allow for the tether to rotate at the attachment point. Again, the relative position feedback is provided by the infrared camera MoCap system, and then the estimation filter using the derated MoCap measurement to imitate the RTK dGPS measurement. The desired relative position is an altitude of 5 and 2.5 m radial distance.

Indoor flight testing builds on the UAV surrogate experiment by including the UAV, thus introducing more variability in the relative position. Because the UAV flies near the ceiling of the indoor testing facility to attain the largest relative altitude, taut tether testing was not performed. The variability of tether tension during taut controller testing is too great and would likely cause the UAV to crash. Therefore, UAV altitude and position variations will be compared to untethered flight. For both the UAV surrogate and indoor flight testing, the limited height of the indoor testing facility resulted in an experiment near the margins of the proposed concept of operation. A scaled-down relative position (5 m altitude vs. 50 m altitude) has less margin for error. For example, a 0.25 m error in tether length has a greater effect when the overall length is 7 m than when it is 60 m.

3.4 | Outdoor flight test setup

For outdoor flight testing, the same 3-PSR wave replication mechanism and UAV were moved outdoors to allow for higher altitude flight, and a more realistic operational scenario. Because the MoCap system does not work well outdoors, nor at the altitude

required, the RTK dGPS payload was added to the UAV as shown in Figure 7. An antenna passes the GPS signal into the dGPS chip which then sends data to a radio. Instead of broadcasting the signal via an antenna, it sends the signal down the RF tether to another radio, and then the dGPS chip attached to the top of the mast on the 3-PSR wave replication mechanism. The mast is connected to one of the mechanism's sliders, raising and lowering in tandem with the smart reel platform, replicating the heave motion. The desired relative position is an altitude of 30 and 15 m radial distance. Outdoor flight testing introduces more complexity such as wind, difficulty in measuring the relative position, and a more realistic deployment environment.

3.5 | Sensing and communication protocol

For autonomous tether management, the developed system needs to sense the dynamics, shape of the tether, and reel in or payout accordingly. The smart reel design is capable of sensing the tether characteristics including instantaneous tether length, tether departure angle, tether tension, and controlling the tether length, as shown in Figure 8. During UAV surrogate testing, the tether tension and arrival angle, β , are sent to the smart reel microprocessor for data syncing via a UDP point to point Ethernet network at 100 Hz. For indoor flight testing, the relative position is measured via the MoCap system, and sent to the smart reel microprocessor via the same Ethernet network at 120 Hz. The data is used in the feedback controller at 50 Hz for purely MoCap feedback, or derated to 4 Hz for Kalman filter estimation feedback. For outdoor flight testing, the airborne dGPS unit sends RTK messages over the tether via a 2.4 GHz radio to the other dGPS unit. The relative position is then transmitted to the smart reel microprocessor via USB serial at 4 Hz for Kalman filter estimation feedback. The specific electronic hardware is listed in Table 1.

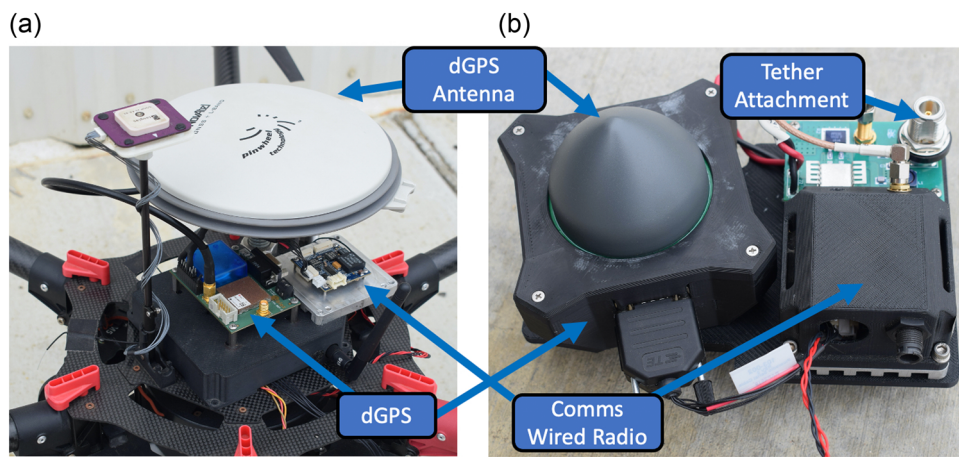


FIGURE 7 Real-time kinetic dGPS payload in: (a) rover mode attached to top of unmanned air vehicle and (b) moving baseline mode attached to the mast on 3-PSR wave replication mechanism. dGPS, differential GPS. [Color figure can be viewed at [wileyonlinelibrary.com](#)]

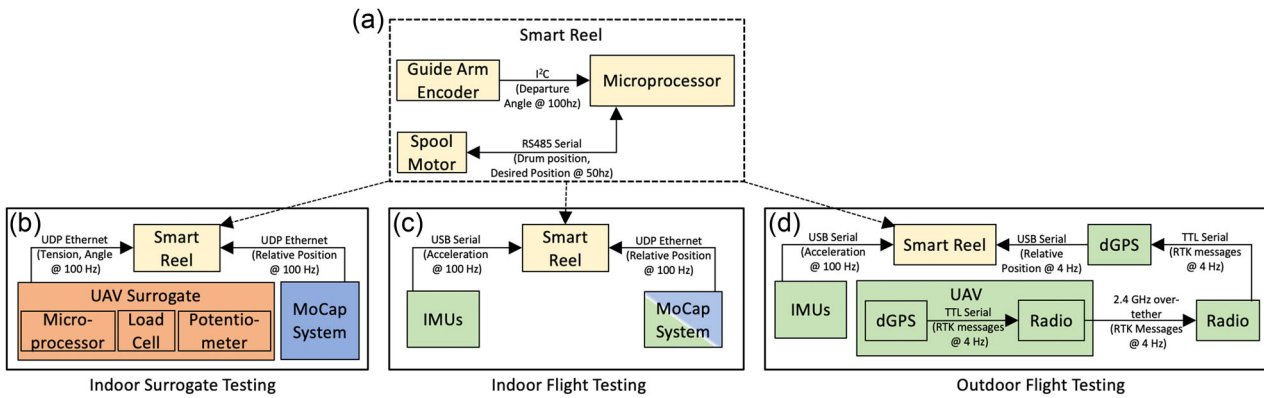


FIGURE 8 Communication protocol diagram for the (a) smart reel, (b) indoor UAV surrogate test setup using purely MoCap feedback, (c) indoor UAV flight test setup using full rate and de-rated MoCap Kalman filter feedback, and (d) Outdoor UAV flight test setup using dGPS Kalman filter feedback. The beige subsystem represents the smart reel. The orange subsystem represents the UAV surrogate. The blue subsystem represents using purely MoCap for feedback. The green subsystem depicts the hardware needed for Kalman filter-based estimation feedback. dGPS, differential GPS; IMU, inertial measurement unit; UAV, unmanned air vehicle. [Color figure can be viewed at [wileyonlinelibrary.com](#)]

TABLE 1 Prototype electronics

Electronics	Supplier	Part Number
UAV surrogate load cell	Loadstar sensor	RAS1-050S-S
UAV surrogate microprocessor	beagleboard	BeagleBone Blue
Smart reel microprocessor	beagleboard	BeagleBone Blue
Smart reel angle arm encoder	US digital	MAE-3
Smart reel spool motor	Moog animatics	SM23165MT
Estimation filter IMU-1	InvenSense	MPU-9250
Estimation filter IMU-2	Lord MicroStrain	3DM-GX5-25
RTK dGPS	u-blox	NEO-M8P-2
dGPS tether radio	Airborne innovations	pDDL2450

Abbreviations: dGPS, differential GPS; IMU, inertial measurement unit; RTK, real-time kinetic; UAV, unmanned air vehicle.

3.6 | Input wave profile

Four distinct wave profiles were developed for testing on the 3-PSR wave replication mechanism. The first profile considered only the heave motion of a wave. The heave-only wave profile was derived from the JONSWAP spectrum (Branlard, 2010). A sum of sinusoidal signals with randomized initial phase was used to create the time series heave profile. The resulting 4 min wave profile had a 1.6 m peak wave amplitude and a 10 s peak period, approximating sea state 3 on the Douglas Sea Scale (Tsai, 1995). The next three wave profiles include heave, pitch, and roll (HPR), and were taken from a Unity engine simulation of a patrol boat using the ultimate water system tool (Unity Technologies, 2017). Each wave had a heave range up to the maximum heave capability of the 3-PSR wave replication mechanism of 2.2 m, pitch range of $\pm 18.1^\circ$, $\pm 14.5^\circ$, $\pm 17.4^\circ$, and roll range of $\pm 16.1^\circ$, $\pm 21.8^\circ$, $\pm 21.1^\circ$, approximating sea state 4. The first two HPR wave profiles were used for tuning the filter, while the last HPR profile was reserved for unbiased testing. The

amplitude of the frequency spectrum for each wave profile and a sample wave profile times series is shown in Figure 9.

4 | EXPERIMENTAL RESULTS

4.1 | UAV surrogate

The UAV surrogate results are presented first using the MoCap system as feedback to validate the controller and mechanical prototype in four parts: tether length, arrival angle, departure angle, and tether tension. Nine separate wave profile trials (three heave-only, three each for two of the HPR profiles) were performed and one stationary, no-motion wave profile to help tune the estimation filter. For comparative testing, each wave profile was also tested with the tension-based controller.

4.1.1 | Tether length

The tether length results for a typical UAV surrogate experiment are shown in Figure 10a. The catenary model-based controller

follows the catenary model-based theory, with a mean error across all runs of 0.022 m and RMSE of 0.028 m as seen in Figure 10b. This shows that the PD controller gains have been tuned well as the actual tether length matches the model. In comparison, the taut controller tether length follows a similar profile, but has an initial offset. The variations are nearly constant with a mean difference of 0.52 m. The catenary model-based control can be interpreted as a tether length buffer for taut control. If the tether length for taut control was known, the same length trend with a longer initial tether length would result in the catenary model-based tether control. However, the initial length difference changes with respect to the relative position between the UAV and USV, thus the catenary model-based controller is necessary.

4.1.2 | Arrival angle, β

The arrival angle, β , of the tether at the UAV surrogate experiments is shown in Figure 11a. The experimental data was filtered with a low-pass filter with a cutoff frequency of 2 Hz to remove the

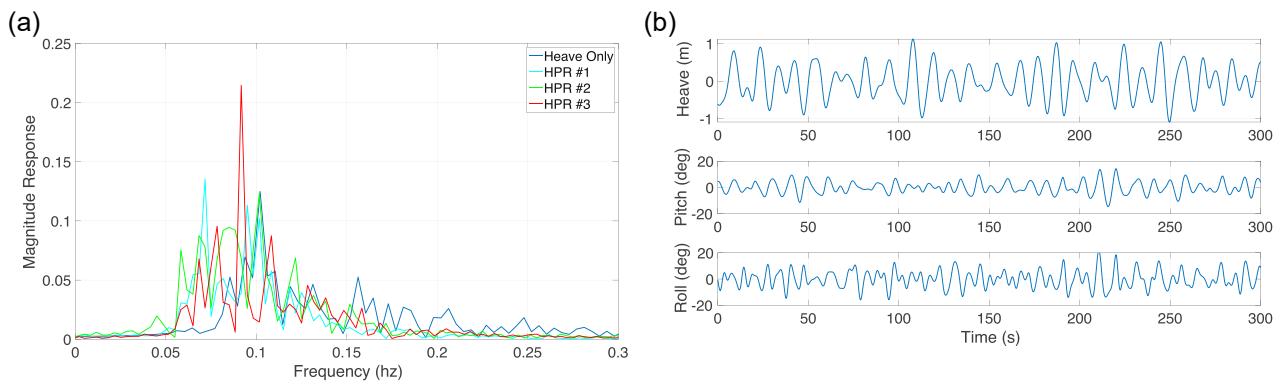


FIGURE 9 Input wave data for the 3-PSR wave replication mechanism. (a) The frequency content of the four wave profiles and (b) time series example of the third wave profile. [Color figure can be viewed at wileyonlinelibrary.com]

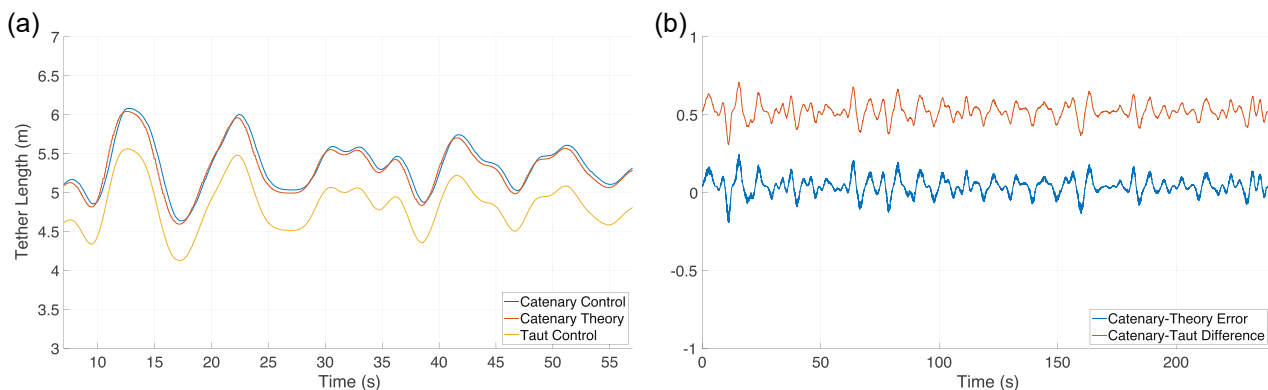


FIGURE 10 Typical tether length experimental results for the unmanned air vehicle surrogate testing. (a) Measured tether length for the taut and catenary model-based control. For reference, the commanded wave height and theoretical catenary model length based on the relative position are also shown. (b) Error between the measured catenary model-based length controller and the theoretical catenary model-based length. Also shown is the difference between the catenary model-based controller and the taut controller. [Color figure can be viewed at wileyonlinelibrary.com]

high-frequency noise inherent in the potentiometer reading. The tether has some elasticity and dynamic effects preventing it from becoming fully taut, resulting in the taut tether angle being slightly greater than the geometric angle. As seen in Figure 11b, the catenary model-based controller followed theory relatively closely, with a mean error of 2.1° , attributable to an initial offset in potentiometer calibration. Interestingly, the taut tether arrival angle shows a similar trend as the catenary model-based controller, as seen by the relatively constant error between the two with a mean error of 12.6° . Similar to the length results, this can be interpreted as the catenary controller providing a constant buffer from the higher tension taut controller. The wave profile has almost the same effect on both test cases, with the main difference being the starting angle.

4.1.3 | Departure angle, γ

The departure angle results of the tether at the smart reel are shown in Figure 12a. The guide arm measurement technique shows promise, but

has a 20° dead-band gap in measurement capability as seen by the periodic vertical lines. This error in measurement occurs when the smart reel switches between reeling in and paying out, and the tether contact point on the follower switch from one side to the other. Improvements to the design of the guide arms and follower may improve the angle measurement. However, this angle measurement design inherently colors the measurement by physically contacting the tether. While a stretching out of the departure angle measurement occurs, the trend still correlates well with the theoretical catenary-based departure angle as seen in the cross correlation in Figure 12b. The normalized correlation peaks at 0.88 s lag, and steadily decreases thereafter. Due to the errors in departure angle measurement, a controller with loop closure based on the reference departure angle was not evaluated.

4.1.4 | Tether tension

Figure 13a shows a typical tether tension result for the catenary model-based control and taut tether control. The tether tension using

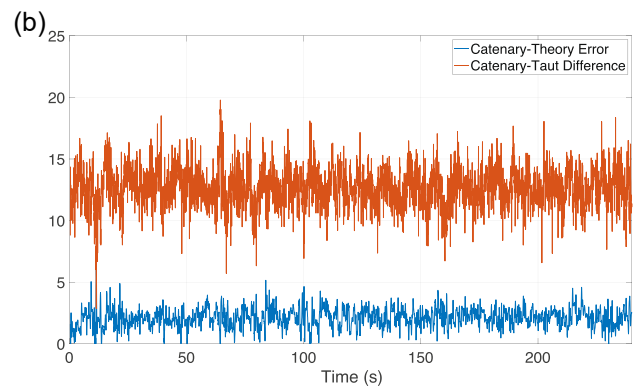
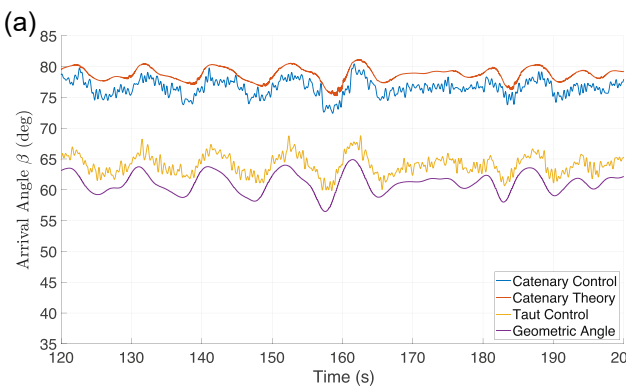


FIGURE 11 Typical arrival angle, β , experimental results for the unmanned air vehicle surrogate testing. (a) Arrival angle showing theoretical catenary angle based on the measured tether length and relative position, the measured angle during catenary control, taut control, and the geometric angle based solely on relative position. (b) Error between theory and the measured angle showing relatively consistent error. The error between catenary measurement and taut measurement is also consistent with minimal variations. [Color figure can be viewed at wileyonlinelibrary.com]

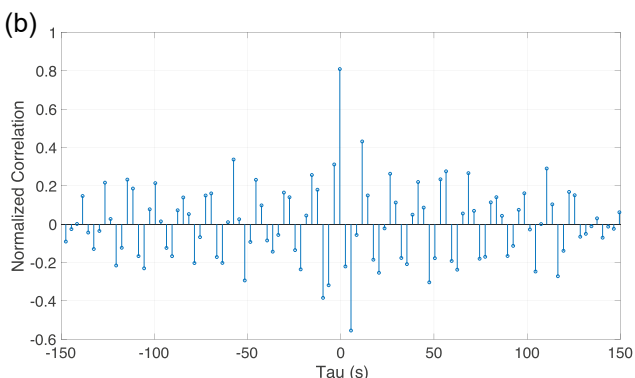
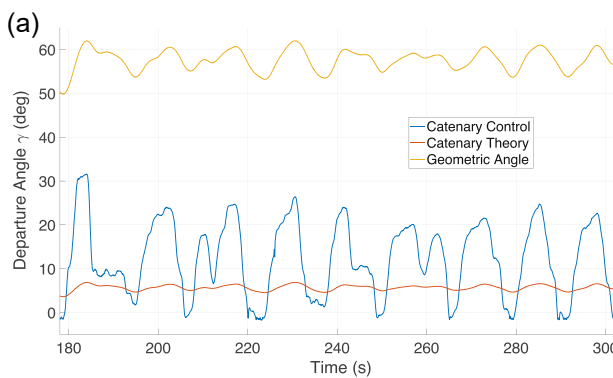


FIGURE 12 Typical departure angle, γ , experimental results for the unmanned air vehicle surrogate testing. (a) Departure angle showing the theoretical angle based on the measured tether length and relative position, the measured angle during catenary control, and the geometric angle based solely on relative position. (b) Normalized cross-correlation between the measured and theoretical departure angles. The two signals are strongly correlated in time as seen by the peak at 0.88 s shift. [Color figure can be viewed at wileyonlinelibrary.com]

the catenary model-based controller had a mean tension of 2.38 N with a standard deviation of 0.27 N. This corresponds well compared to the theoretical tension based on the measured relative position and tether length. The mean error between the experimental and theory was 0.08 N with a standard deviation of 0.20 N as seen in Figure 13b. This shows that the controller minimized the dynamic effects of tether motion on the UAV in a controlled environment, while having perfect feedback and no external disturbances such as wind. The taut controller had a significantly higher mean tether tension of 27.52 N, with a much larger standard deviation of 7.30 N. Perhaps more significant is the peak-to-peak variation of 2.21 N for catenary control and 55.70 N for taut tether control, showing the greater variability of tension for the taut controller. Some of the taut tension variability can be attributed to the friction inherent in the spooling system. The torque setting on the spool motor had to be above the friction-stiction threshold to ensure continuous motion and prevent undesired stiction on the drum. A mechanical clutch or other tension sensing method has been shown to limit tension to a more consistent 8 N force, but not to the minimized level of the catenary model-based controller (Briggs & Stave, 2017).

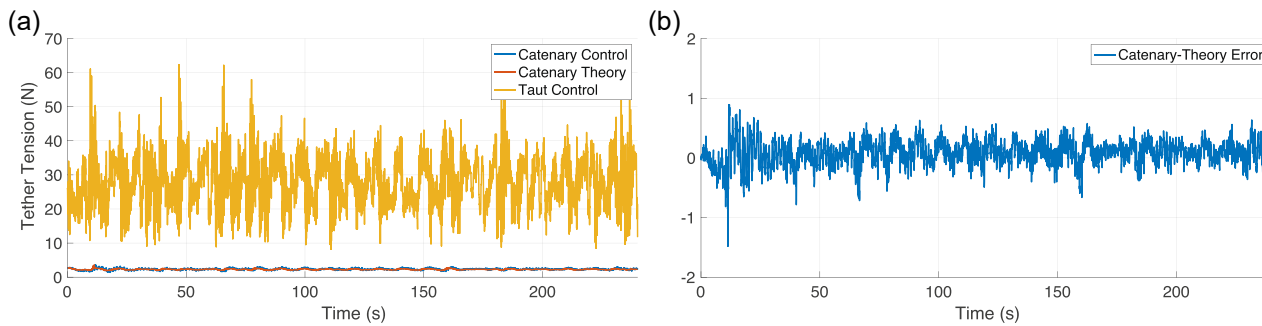


FIGURE 13 Typical experimental unmanned air vehicle surrogate tether tension results. (a) Tether tension for both taut and catenary model-based controllers for the same wave profile. The theoretical catenary tether tension based on measured relative position and tether length corresponds well with the experimental catenary controller. (b) Error between the catenary model-based controller and the theoretical values. [Color figure can be viewed at wileyonlinelibrary.com]

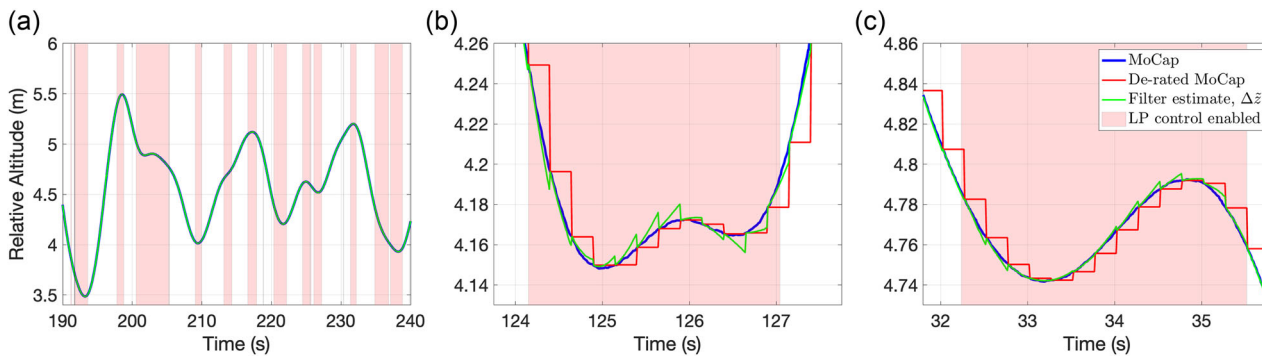


FIGURE 14 Twiddle Algorithm relative altitude tuning results for (a) a 50 s time frame of HPR wave profile # 2, (b) a 4 s time frame of the heave-only profile, and (c) a 4 s time frame of HPR wave profile # 2. The 50 s segment shows the estimation filter tracking the ground truth MoCap measurements. The close-up views also show the 4 Hz de-rated MoCap measurements. The filter fills in the gaps between measurements, but has some errors when the wave profile slows down and changes directions, particularly bad for the heave-only profile. HPR, heave, pitch, and roll. [Color figure can be viewed at wileyonlinelibrary.com]

4.2 | Estimation filter

The estimation filter tuning results are presented first for the nine wave motion trials and one stationary motion trials using MoCap data as ground truth. The filter is then evaluated through an additional eight wave profile trials using the output of the filter as feedback for control.

4.2.1 | Estimation filter tuning

Using the Twiddle Algorithm, the standard deviation gains on the filter were tuned to $\sigma_z = 0.0133$, $\sigma_{\dot{z}} = 8.66e - 08$, $\sigma_{\ddot{z}} = 0.453$, $\sigma_{\mu_1} = 1.473$, $\sigma_{\mu_2} = 0.0146$, $\sigma_{\Delta\dot{z}_{Acc_1}} = 112.94$, $\sigma_{\Delta\dot{z}_{Acc_2}} = 91.105$, and when a relative position measurement exists, $\sigma_{\Delta z_{dGPS}} = 0.01$, otherwise $\sigma_{\Delta z_{dGPS}} = \infty$. Figure 14a shows a typical result for one of the HPR wave profiles. The filter properly fills in the gaps between the de-rated MoCap measurements, but has some overshoot errors when the wave profile slows down and changes direction as seen in the shaded regions, shown scaled up in Figure 14b,c. The overshoot errors are

particularly bad on the heave-only profile. They are attributed to actuator noise and resonance of the three stepper motors on the 3-PSR wave replication mechanism actuating in unison. This is also clearly seen in the mean error and RMSE error shown in Table 2, as the filter error for the heave-only profile is double that of the other wave profiles. For comparison, the tuned estimation filter outperforms a first-order hold (FOH) estimate using only the derated MoCap measurements for all but the stationary motion profile. To account for the errors and overshoot seen when the relative velocity is low, the relative velocity gain-scheduled low-pass filter was implemented on the commanded tether length as previously discussed in Section 2.2. The relative velocity for the same wave profiles is shown in Figure 15.

TABLE 2 Estimation filter error

	Heave-only	HPR # 1	HPR # 2	Minimal motion
Test time (s)	883.5	1027.8	1032.8	837.4
$\Delta\dot{z}$ Mean IErrorl (m)	0.00256	0.00135	0.00144	0.00111
$\Delta\dot{z}$ RMSE (m)	0.00418	0.00239	0.00228	0.00298
FOH mean IErrorl (m)	0.00488	0.00280	0.00291	0.0007
FOH RMSE (m)	0.00783	0.00439	0.00443	0.0018

Abbreviations: FOH, first-order hold; HPR, heave, pitch, and roll; RMSE, root mean square error.

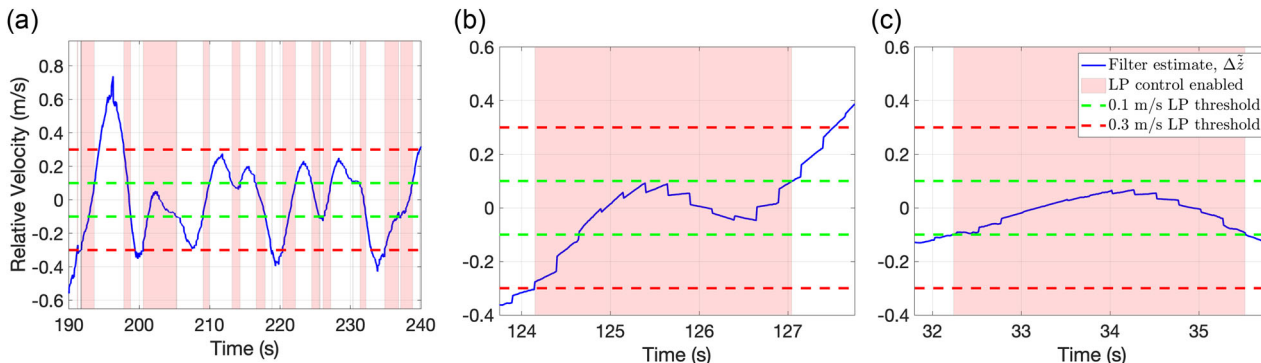


FIGURE 15 Typical Twiddle Algorithm relative velocity tuning results for the same (a) 50 s time frame of HPR wave profile # 2, (b) 4 s time frame of the heave-only profile, and (c) 4 s time frame of HPR wave profile # 2. The 0.1 and 0.3 m/s gain-scheduling thresholds for the low-pass filter are shown, and the shaded region where the low-pass filter is active. HPR, heave, pitch, and roll. [Color figure can be viewed at wileyonlinelibrary.com]

TABLE 3 Tether length error

	Heave-only	HPR # 1	HPR # 2	HPR # 3	Total
Test time (s)	514.76	648.04	657.11	645.52	2,465.43
Mean IErrorl (m)	0.022	0.019	0.023	0.024	0.022
RMSE (m)	0.027	0.024	0.028	0.029	0.027

Abbreviations: HPR, heave, pitch, and roll; RMSE, root mean square error.

The gain-scheduling for the low-pass filter activates the filter at two different thresholds, as seen in the heave-only profile activating at a threshold of -0.3 m/s at 124.2 s, and the HPR wave profile activating at a threshold of 0.1 m/s at 32.5 s. The lower magnitude threshold activates if the relative velocity has not gone above the higher magnitude threshold, as seen in the longer HPR profile view between 210 and 218 s. As seen in the shaded region in Figure 14, the gain-scheduler accurately activates the low-pass filter when the relative position errors are largest. The effects of this gain-scheduled low-pass filtering on the tether length will be discussed in the next section.

4.2.2 | Estimation filter feedback control

To evaluate the tuned estimation filter performance for feedback control, eight experimental trials were performed, two for each wave profile, including the HPR #3 profile which was not used to tune the filter. Table 3 shows the mean error and RMSE error of the tether length compared to the ideal tether length if MoCap has been used for feedback. The gain-scheduled controller worked well across all wave profiles with a mean error of 0.022 m and RMSE of 0.027 m , only slightly different than for the MoCap feedback presented in Section 4.1.1.

Further motivating the need for the gain-scheduled low-pass tether reference length, Figure 16a shows a typical tether length result close up view for one of the HPR #3 trials. When the gain-scheduler changes α from 1 to 0.2, denoted by the shaded region, the commanded tether length transitions from the purely estimation

filter-based tether reference length signal to the low-pass filtered tether reference length signal. In doing so, the discontinuities and oscillations present in the estimation filter-based tether reference length signal seen in the shaded region do not propagate through to the commanded tether length. The oscillations in the estimation filter tether reference length generally occurred more when slowing down into a change in direction than when speeding up out of the change in direction. This motivated the dual-threshold gain-scheduler, allowing the commanded signal to speed up earlier when exiting the low-pass enabled region as seen by the actual tether length after 51.5 s, where it coincides with the low-pass tether reference length signal. In contrast, Figure 16b shows a typical result for another trial where the gain-scheduled low-pass filter was not enabled. The commanded tether reference length signal retains the discontinuities and oscillations from the estimation filter, which ultimately manifests as

oscillations in the actual tether length, visibly noticeable on the smart reel. Figure 16c shows the frequency spectrum content of the actual tether length for both trials. The low-pass gain-scheduled controller removes the 4 Hz frequency content from the tether length output. A downside of implementing the low-pass filter is a small lag as is seen by the main peak of the frequency content occurring at a slightly lower frequency for the low-pass filtered trial. However, the low-pass filter is gain-scheduled to only activate when it is needed, when the relative velocity is low, mitigating the lag effects as much as possible.

4.3 | Indoor flight

Typical experimentation images of one period of a 1.9 m wave of a HPR wave profile trial are shown in Figure 17. The tether is

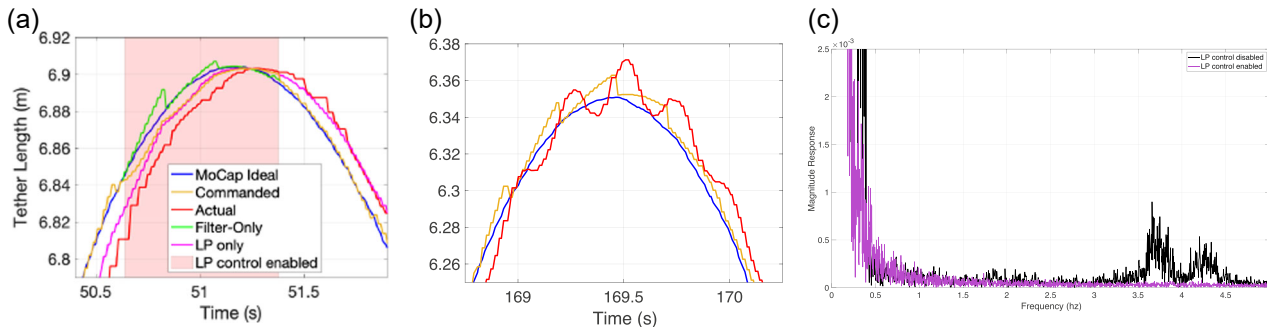


FIGURE 16 Typical tether length results from HPR wave profile # 3 using the estimation filter as feedback showing (a) a close up view of the low-pass gain-scheduler activating, transitioning from using purely estimation filter-based tether reference length to a low-pass filter-based tether reference length and back, (b) a close up view for a trial run without the low-pass gain-scheduler, and (c) the frequency content of the actual tether length from (a) and (b). HPR, heave, pitch, and roll. [Color figure can be viewed at wileyonlinelibrary.com]

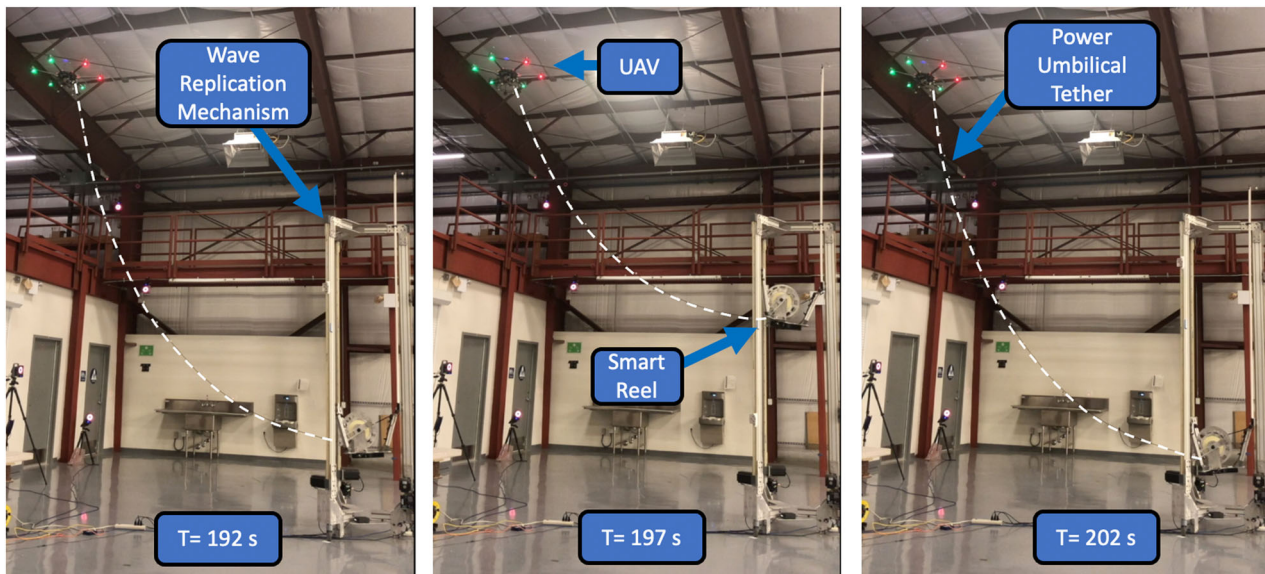


FIGURE 17 Typical experimental indoor flight testing for a single wave period during an HPR #2 wave profile trial at 192, 197 and 202 s duration. The tether has been highlighted with a white dashed line to make it more visible. Notice the tether is not taut and resembles a catenary curve. HPR, heave, pitch, and roll. [Color figure can be viewed at wileyonlinelibrary.com]

highlighted with a dashed line to make it more visible. The catenary model-based control performed well, with the tether remaining in the shape of a catenary curve throughout the large heave motion. The tether was instrumented with 11 motion capture spheres, or nodes, as seen in Figure 18. The dynamics of the tether motion produced a mean positional error from the catenary theory-based reference shape of 0.076 m over eight separate trials (two per wave profile), with a standard deviation of 0.0378 m. The reaction time of the smart reel is fast enough to mitigate any dynamic effects due to UAV and smart reel motion.

The altitude displacement of the UAV during a typical experiment is shown in Figure 19a. Because there was no position feedback on the UAV flight controller for station keeping, the RC pilot was

required to hold altitude and position manually, which proved challenging in the confined testing space. The UAV altitude fluctuated 1.08 m from peak to peak, with a standard deviation of 0.18 m across the eight separate wave motion trials. The UAV position stayed within a circular radius of 0.60 m across all trials. To better gauge the effects of the tether, one untethered flight was performed in the same location. For the untethered flight, the altitude fluctuated 0.99 m peak to peak, with a standard deviation of 0.18 m, and positional motion within a radius of 0.48 m, on par with that for tethered flight. This range of motion is within the realm of what a standard UAV flight controller can do using GPS and barometer control outdoors (Hoffmann et al., 2017; Holman et al., 2017). To further demonstrate the decoupling of the UAV and USV motion, the

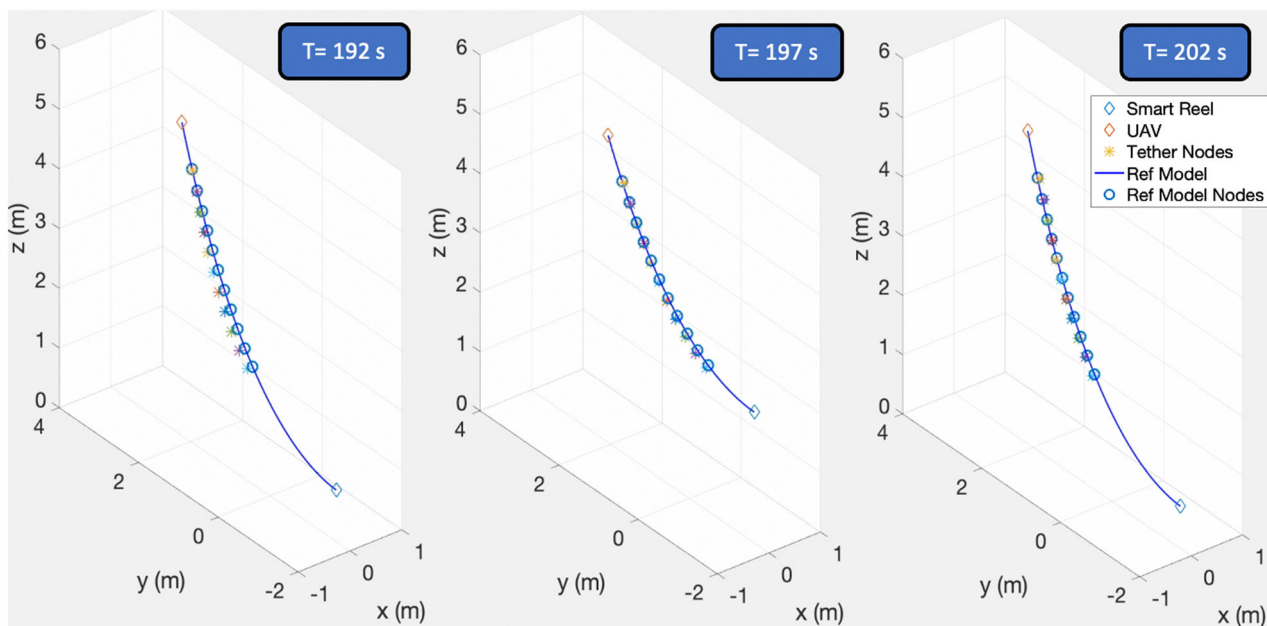


FIGURE 18 Typical experimental indoor flight testing MoCap for a single wave period during an HPR #2 wave profile trial at 192, 197, and 202 s duration. Eleven nodes on the tether, as well as the unmanned air vehicle and smart reel locations demonstrate a catenary-shaped hanging curve. The theoretical reference catenary curve and the corresponding nodal points are shown for comparison. HPR, heave, pitch, and roll. [Color figure can be viewed at [wileyonlinelibrary.com](#)]

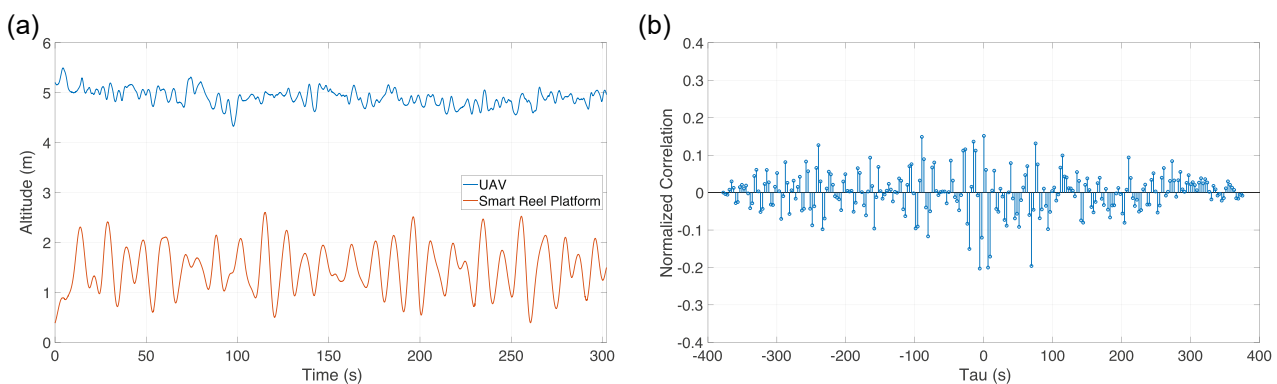


FIGURE 19 Typical altitude results for indoor flight testing for HPR #2. (a) UAV altitude and smart reel platform height for a typical experiment. (b) Normalized cross-correlation between UAV altitude and smart reel platform height. The low correlation demonstrates a successful decoupling of UAV flight from the USV motion. HPR, heave, pitch, and roll; UAV, unmanned air vehicle. [Color figure can be viewed at [wileyonlinelibrary.com](#)]

normalized cross-correlation of the measured altitude and wave height is shown in Figure 19b. The amplitude of the cross-correlation is relatively flat for all time shifts, under a normalized 0.2. If the tether were pulling on the UAV, a peak near-zero lag would be expected. The error statistics for the estimation filter and the tether controller for the indoor flight trials are shown in Table 4. Noticeably, the mean error and RMSE for the estimation filter are three to four times greater than those shown in Table 2. With the addition of the UAV, both endpoints of the tether are now dynamically moving, resulting in a some larger estimation errors. However, these errors are again relegated to the regions of the smart reel changing directions. The key error metric is the tether length error, which has improved compared to the UAV surrogate testing as shown in Table 3. The UAV having the ability to move dynamically adds a factor of compliance, while the smart reel decouples large-scale motions. The gain-scheduled low-pass filter performs well in preventing errors and discontinuities in the estimation filter from propagating through to the tether length.

In summary, the catenary model-based tether control allows the UAV to hold position and altitude within the bounds of what an RC

pilot can achieve. The gain-scheduled low-pass filter successfully mitigates any discontinuities realized in the estimation filter at low speeds. The smart reel successfully decouples the motion of the UAV and USV, while also minimizing induced dynamics on the tether.

4.4 | Outdoor flight

Typical experimentation images of one period of a 1.7 m wave are shown in Figure 20. The tether is highlighted with a dashed line to make it more visible. The catenary model-based control performed well over eight separate trials (two per wave), with the tether remaining in the shape of a catenary curve throughout the wave motion. Most notably, compared to the scenario where the tether management controller is turned off, the tether sags below the smart reel and would be fouled in a real deployment scenario.

In switching from the MoCap system to the RTK dGPS system, a few technical challenges needed to be addressed. Figure 21a shows the relative altitude output from the estimation filter and the raw dGPS measurements for a HPR #2 trial run. Notice that the Kalman filter fills in the gaps between the dGPS measurements reasonably well. However, as seen at 98.75 s, the RTK dGPS system used was not completely reliable, and failed to produce a message. This missed message incident occurred at a rate of 1.35%. When the dGPS failed to produce a message, the estimation filter kept dead reckoning using the inertial measurements as desired. However, the following dGPS measurement was often stale and incorrect, as seen at 99.5 s. The missed dGPS measurements required one second in order for dGPS system to sort itself out before outputting a good message, occasionally producing a completely erroneous measurement, as seen at 113.5 s. As seen in Figure 21b for a HPR #3 trial run, logic was implemented to make sure the change in dGPS message

TABLE 4 Indoor flight estimation filter and tether length error

	Heave-only	HPR # 1	HPR # 2	HPR # 3
Test time (s)	512.4	669.1	627.8	605.5
$\Delta\hat{z}$ Mean Error (m)	0.0082	0.0056	0.0054	0.0058
$\Delta\hat{z}$ RMSE (m)	0.012	0.0083	0.0080	0.0087
L Mean Error (m)	0.0118	0.0096	0.0100	0.0099
L RMSE (m)	0.0163	0.0132	0.0135	0.0135

Abbreviations: HPR, heave, pitch, and roll; RMSE, root mean square error.

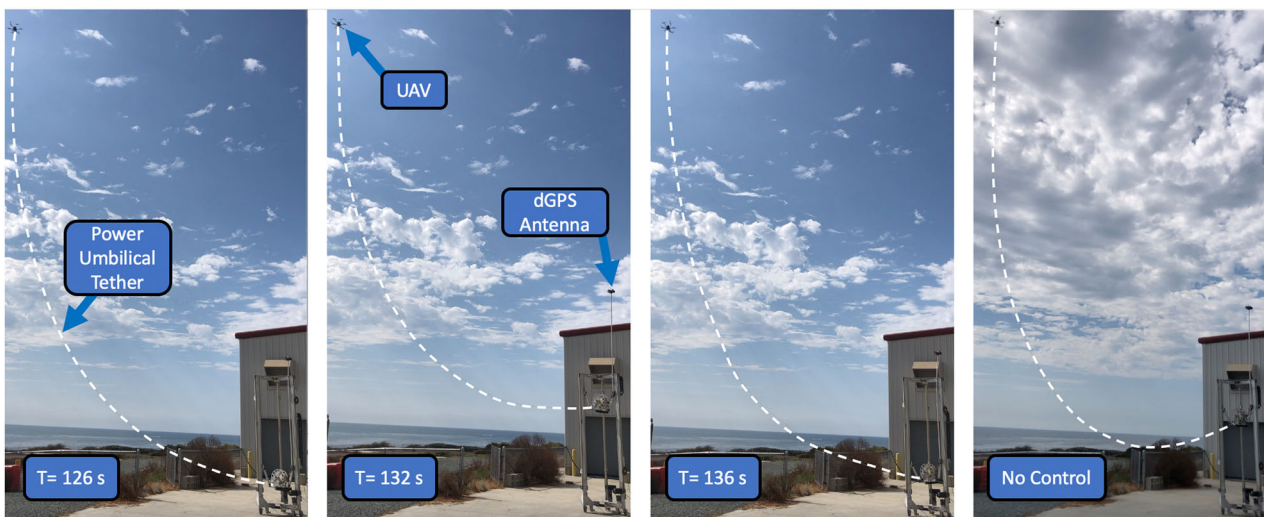


FIGURE 20 Typical outdoor flight testing for HPR #3 at 126, 132, 136 s, and no control. The tether has been highlighted with the white dashed line to make it more visible. Notice the tether is not taut, and resembles a catenary curve when the controller is active, whereas the tether has sagged below the platform when no controller is active. HPR, heave, pitch, and roll; UAV, unmanned air vehicle. [Color figure can be viewed at wileyonlinelibrary.com]

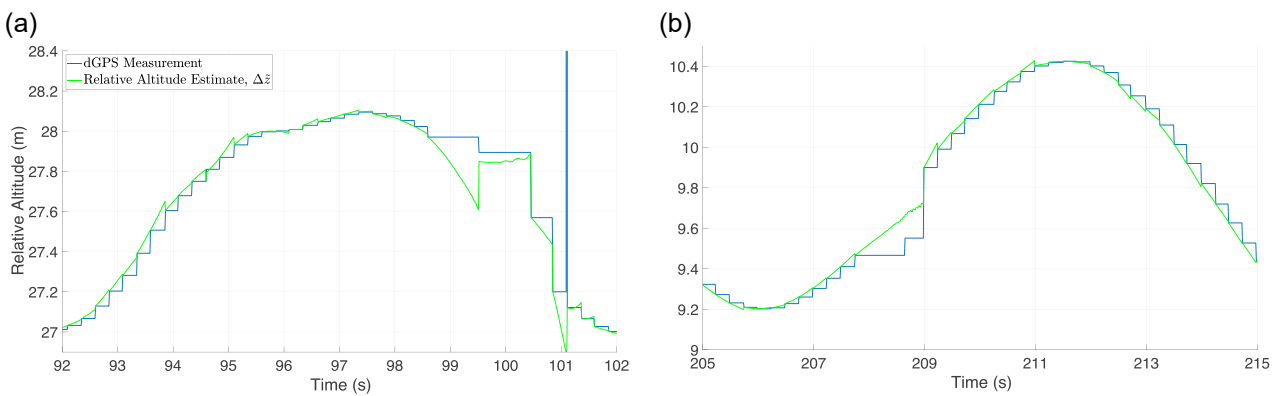


FIGURE 21 Typical relative altitude results for an outdoor flight for (a) an HPR #2 trial showing the relative altitude comparing dGPS and estimation filter output for a typical experiment before logic and time stamp checks were implemented. Note the errors in the dGPS measurements surrounding 100 s. A dGPS message is missed or unavailable at 98.75 s, and then a stale message arrives at 99.5 s. Then another stale message arrives at 100.5 s and the messages are correct at 100.75 s, with an erroneous message at 101 s. (b) an HPR #3 trial showing a similar output after dGPS message logic and time stamp checks were applied. Note the missed dGPS message at 207.75 s and the stale message at 208.65 s does not adversely affect the Kalman filter output. dGPS, differential GPS; HPR, heave, pitch, and roll. [Color figure can be viewed at [wileyonlinelibrary.com](#)]

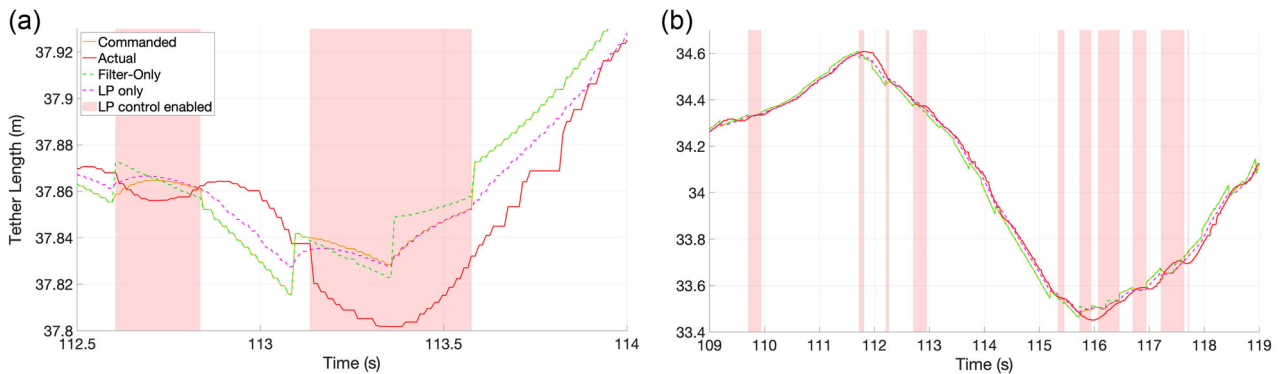


FIGURE 22 Typical tether length results for an outdoor flight for (a) an HPR #3 trial showing the commanded and actual tether length and (b) an HPR #2 trial showing the commanded and actual tether length for a longer, 10 s section. HPR, heave, pitch, and roll. [Color figure can be viewed at [wileyonlinelibrary.com](#)]

timestamps were in line with the change in time from the microprocessor. The missed dGPS message at 207.75 s and the stale message at 208.65 s does not affect the Kalman filter output. Additional logic was implemented to prevent any change in subsequent dGPS measurements greater than 1 m from being used in the estimation filter. With the addition of logic, the dGPS Kalman filter estimation is a reasonable solution for outdoor operation.

Typical tether length results are shown in Figure 22a for a short 1.5 s section of a HPR #3 trial. Between 113.2 and 113.6 s, the low-pass filter activates, and the discontinuities shown in the filter-only output are avoided. When the low-pass filter deactivates at 113.6 s and the wave profile speeds up, the lag in the actual tether length decrease as seen by the decreasing gap between the filter only output and the actual tether length. Figure 22b shows a longer, 10 s section of a HPR #2 trial. Notice that the actual tether length stays relatively smooth, with the low-pass filter activating when the relative velocity is low. While the results for the outdoor flight testing are harder to analyze since there is no ground truth measurement to

base an idealized tether length off, the control scheme shows promise.

5 | SUMMARY AND CONCLUSION

A semislack, hanging tether model for tether management of a UAV-USV team was implemented and experimentally validated with a prototype smart reel in a controlled and relevant dynamic environment. The developed prototype smart reel, capable of measuring the tether length, departure angle, and tension, shows promise in using the angle measurement for feedback, but the tether length alone was ultimately used as the most reliable, accurate measurement. The semislack hanging tether model, dependent on the relative position between the UAV and USV was extended to operate through a larger relative position range, extending above $\Delta r/\Delta z > 1.2$. With the goal of outdoor operation, a Kalman filter model was developed to combine a slow, 4 Hz, RTK dGPS relative

position measurement with fast, 100 Hz inertial measurements, to output a fast, 100 Hz estimate of the relative position, relative velocity, and inertial sensor bias. The estimation filter was tuned using experimental data from an indoor MoCap system as a ground truth measurement. A relative velocity-based gain-scheduled controller was developed and experimentally validated through three experimental phases: surrogate, indoor flight, and outdoor flight testing.

Experimental testing with a UAV surrogate showed that the controller works well in a controlled environment with no external disturbances. The tether tension agreed closely with the predicted values from catenary theory. More importantly, taut tether control exhibits 12 times more tether tension. The tether length trend for both the taut and catenary model-based control were similar, but had an initial offset. If the taut tether length was known, an offset buffer would create the same effect. However, that buffer changes depending on the relative position, that is, the model, controller, and estimation filter are necessary.

Indoor flight testing showed that the catenary controller works well with a UAV at large, dynamically varying relative positions. No correlation between the UAV and USV's altitude was detected, demonstrating effective decoupling of their respective motions. Additionally, the UAV's range of motion was comparable to that of untethered flight. The RC pilot was able to perform manual station keeping comparable to that of a GPS controller. Outdoor flight in a representative operational environment showed good results using the RTK dGPS and IMU Kalman filter for relative position feedback, as long as some logic was implemented to ensure the RTK dGPS messages were proper.

For most tethered UAV operational scenarios, one of the ultimate goals is to fly at high altitude. The higher the UAV flies, the more the tether pulls down on the UAV, and the larger thrust authority and margin are required. This tether management system ultimately decreases the safety margins, allowing for higher UAV flight up to and above 50 m, as well as flying from a USV in moderate seas. A major benefit of this control system is that it is based purely on relative position, regardless of scale.

Further work is needed to quantify disturbance effects, especially those from wind and GPS drift. An extensive set of follow-on experimental tests is planned and currently underway, including controlled environment sea trials at Naval Surface Warfare Center's Maneuvering and Seakeeping Basin facility, and representative ocean sea trials. A follow on article will detail the experimental findings once adequately performed, analyzed, and approved for release. Lastly, because the model is dependent on the static formulation of hanging tether theory, a dynamic model formulation and simulation environment may be able to capture the rich dynamic of the tether, and lead the way for more advantageous model-based controllers. This is especially important and relevant for GPS denied operational concepts. Follow on work to develop a dynamic model and simulation environments is also underway.

ACKNOWLEDGMENTS

This study was supported by Naval Information Warfare Center Pacific under the Naval Innovative Science and Engineering program, and the Department of Defense SMART Scholarship for Service program.

DATA AVAILABILITY STATEMENT

The data that support the findings of this study are available from the corresponding author upon reasonable request.

REFERENCES

- Abbeel, P., Coates, A., Montemerlo, M., Ng, A.Y. & Thrun, S. (2005) Discriminative training of Kalman filters. In: *Robotics: Science and systems*, Vol. 2, p. 1.
- Ahmed, B. & Pota, H.R. (2008) Backstepping-based landing control of a RUAV using tether incorporating flapping correction dynamics. In: 2008 American Control Conference, pp. 2728–2733.
- Al-Radaideh, A. & Sun, L. (2017) Self-localization of a tethered quadcopter using inertial sensors in a GPS-denied environment. In: 2017 International Conference on Unmanned Aircraft Systems (ICUAS), pp. 271–277.
- Branlard, E. (2010) Generation of time series from a spectrum. TU Denmark.
- Briggs IV, F.M. & Stave, T. (2017) Reactive tether spool. US Patent App. 15/456,096.
- Carvalho, H., Del Moral, P., Monin, A. & Salut, G. (1997) Optimal nonlinear filtering in GPS/INS integration. *IEEE Transactions on Aerospace and Electronic Systems*, 33(3), 835–850.
- Choi, S.Y., Choi, B.H., Jeong, S.Y., Gu, B.W., Yoo, S.J. & Rim, C.T. (2014) Tethered aerial robots using contactless power systems for extended mission time and range. In: 2014 IEEE Energy Conversion Congress and Exposition (ECCE), pp. 912–916.
- Ferreira de Castro, D., Santos, J.S., Batista, M., AntôniodosSantos, D. & Góes, L.C. (2015) Modeling and control of tethered unmanned multicopters in hovering flight. In: *AIAA Modeling and Simulation Technologies Conference*. American Institute of Aeronautics and Astronautics.
- Galea, B. & Kry, P.G. (2017) Tethered flight control of a small quadrotor robot for stippling. In: 2017 IEEE/RSJ International Conference on Intelligent Robots and Systems (IROS), pp. 1713–1718.
- Gross, J.N., Gu, Y. & Rhudy, M.B. (2015) Robust UAV relative navigation with DGPS, INS, and peer-to-peer radio ranging. *IEEE Transactions on Automation Science and Engineering*, 12(3), 935–944.
- Hoffmann, G., Huang, H., Waslander, S. & Tomlin, C. (2007) Quadrotor helicopter flight dynamics and control: theory and experiment. In: *AIAA Guidance, Navigation and Control Conference and Exhibit*, p. 6461.
- Holman, R.A., Brodie, K.L. & Spore, N.J. (2017) Surf zone characterization using a small quadcopter: technical issues and procedures. *IEEE Transactions on Geoscience and Remote Sensing*, 55(4), 2017–2027.
- Kim, J., Song, B.D. & Morrison, J.R. (2013) On the scheduling of systems of UAVs and fuel service stations for long-term mission fulfillment. *Journal of Intelligent & Robotic Systems*, 70(1), 347–359.
- Kiribayashi, S., Yakushigawa, K. & Nagatani, K. (2017) Position estimation of tethered micro unmanned aerial vehicle by observing the slack tether. In: 2017 IEEE International Symposium on Safety, Security and Rescue Robotics (SSRR), pp. 159–165.
- Lupashin, S. & D'Andrea, R. (2013) Stabilization of a flying vehicle on a taut tether using inertial sensing. In: 2013 IEEE/RSJ International Conference on Intelligent Robots and Systems, pp. 2432–2438.

- Nicotra, M.M., Naldi, R. & Garone, E. (2014) Taut cable control of a tethered UAV. *IFAC Proceedings Volumes*, 47(3), 3190–3195. 19th IFAC World Congress.
- Nicotra, M.M., Naldi, R. & Garone, E. (2016) Nonlinear control of a tethered UAV: the taut cable case. CoRR.
- Oh, S. (2010) Multisensor fusion for autonomous UAV navigation based on the unscented Kalman filter with sequential measurement updates. In: 2010 IEEE Conference on Multisensor Fusion and Integration, pp. 217–222.
- Oh, S.-R., Pathak, K., Agrawal, S.K., Pota, H.R. & Garratt, M. (2006) Approaches for a tether-guided landing of an autonomous helicopter. *IEEE Transactions on Robotics*, 22(3), 536–544.
- Ouchi, Y., Kinoshita, K., Watanabe, K. & Nagai, I. (2014) Control of position and attitude of the tethered X4-Flyer. In: 2014 IEEE/SICE International Symposium on System Integration, pp. 706–711.
- Papachristos, C. & Tzes, A. (2014) The power-tethered UAV-UGV team: a collaborative strategy for navigation in partially-mapped environments. In: 22nd Mediterranean Conference on Control and Automation, pp. 1153–1158.
- Prior, S.D. (2015) Aether - persistent aerial surveillance using a small unmanned aircraft system. In: 15th Annual Conference on Unmanned Aerial Systems.
- Qi, H. & Moore, J.B. (2002) Direct Kalman filtering approach for GPS/INS integration. *IEEE Transactions on Aerospace and Electronic Systems*, 38(2), 687–693.
- Sandino, L., Bejar, M., Kondak, K. & Ollero, A. (2014) Advances in modeling and control of tethered unmanned helicopters to enhance hovering performance. *Journal of Intelligent & Robotic Systems*, 73(1), 3–18.
- Sandino, L.A., Bejar, M., Kondak, K. & Ollero, A. (2013) On the use of tethered configurations for augmenting hovering stability in small-size autonomous helicopters. *Journal of Intelligent & Robotic Systems*, 70(1), 509–525.
- Sandino, L.A., Bejar, M., Kondak, K. & Ollero, A. (2015) A square-root unscented Kalman filter for attitude and relative position estimation of a tethered unmanned helicopter. In: 2015 International Conference on Unmanned Aircraft Systems (ICUAS), pp. 567–576.
- Sandino, L.A., Santamaria, D., Bejar, M., Viguria, A., Kondak, K. & Ollero, A. (2014) Tether-guided landing of unmanned helicopters without GPS sensors. In: 2014 IEEE International Conference on Robotics and Automation (ICRA), pp. 3096–3101.
- Schall, G., Wagner, D., Reitmair, G., Taichmann, E., Wieser, M., Schmalstieg, D. & Hofmann-Wellenhof, B. (2009) Global pose estimation using multi-sensor fusion for outdoor augmented reality. In: 2009 8th IEEE International Symposium on Mixed and Augmented Reality, pp. 153–162.
- Schmidt, G. & Swik, R. (1974) Automatic hover control of an unmanned tethered rotorplatform. *Automatica*, 10(4), 393–394.
- Schmitt, O.H. (1938) A thermionic trigger. *Journal of Scientific Instruments*, 15(1), 24–26.
- Simon, D. (2006) *Optimal state estimation: Kalman, H infinity, and nonlinear approaches*. John Wiley & Sons.
- Suhr, J.K., Jang, J., Min, D. & Jung, H.G. (2017) Sensor fusion-based low-cost vehicle localization system for complex urban environments. *IEEE Transactions on Intelligent Transportation Systems*, 18(5), 1078–1086.
- Talke, K., Drotman, D., Stroumtsos, N., Oliveira, M. & Bewley, T. (2019) Design and parameter optimization of a 3-PSR parallel mechanism for replicating wave and boat motion. In: 2019 IEEE International Conference on Robotics and Automation (ICRA).
- Talke, K., Oliveira, M. & Bewley, T. (2018) Tether shape analysis for a UAV - USV team. In: 2018 IEEE International Conference on Intelligent Robots (IROS).
- Thrun, S. (2012) The twiddle algorithm is attributed here to Sebastian Thrun, in lectures through the Udacity programme. <https://www.youtube.com/watch?v=2uQ2BSzDvXs>.
- Thrun, S., Burgard, W. & Fox, D. (2005) *Probabilistic robotics*. MIT Press.
- Tognon, M., Dash, S.S. & Franchi, A. (2016) Observer-based control of position and tension for an aerial robot tethered to a moving platform. *IEEE Robotics and Automation Letters*, 1(2), 732–737.
- Tsai, L.-W. (1995) *Marine observer's handbook*, 8th ed: HMSO.
- Unity Technologies. (2017) Unity. <https://unity3d.com/get-unity/download/archive>, <https://assetstore.unity.com/packages/3d/vehicles/sea/patrol-boat-46913>, <https://assetstore.unity.com/packages/tools/particles/efcts/uws-ultimate-water-system-100669>. Version 2017.2.0f3.
- Zikou, L., Papachristos, C. & Tzes, A. (2015) The power-over-tether system for powering small UAVs: tethering-line tension control synthesis. In: 2015 23rd Mediterranean Conference on Control and Automation (MED), pp. 681–687.

SUPPORTING INFORMATION

Additional supporting information can be found online in the Supporting Information section at the end of this article.

How to cite this article: Talke, K., Birchmore, F. & Bewley, T. (2022) Autonomous hanging tether management and experimentation for an unmanned air-surface vehicle team. *Journal of Field Robotics*, 1–19.

<https://doi.org/10.1002/rob.22083>